Check for updates

*Magnetic Resonance in Medicine*

WILEY | ISMRM ONE COMMUNITY FOR CLINICIANS AND SCIENTISTS

TECHNICAL NOTE

# Assessment of Lung Microvasculature Alterations in Pulmonary Fibrosis With Hyperpolarized Xenon Magnetic Resonance

Ming Zhang[1,2] | Haidong Li[1,2] | Hongchuang Li[1,2] | Xiuchao Zhao[1,2] | Xiaoling Liu[1,2] | Yu Zheng[1,2] | Yeqing Han[1,2] | Chuan Qin[3] | Xin Zhou[1,2,4]

[1]State Key Laboratory of Magnetic Resonance Spectroscopy and Imaging, National Center for Magnetic Resonance in Wuhan, Wuhan Institute of Physics and Mathematics, Innovation Academy for Precision Measurement Science and Technology, Chinese Academy of Sciences, Wuhan, China | [2]University of Chinese Academy of Sciences, Beijing, China | [3]Tongji Hospital, Tongji Medical College, Huazhong University of Science and Technology, Wuhan, China | [4]School of Biomedical Engineering, Hainan University, Haikou, China

**Correspondence:** Xin Zhou (xinzhou@wipm.ac.cn)

**Received:** 4 August 2025 | **Revised:** 8 January 2026 | **Accepted:** 19 January 2026

**Keywords:** gas exchange | hyperpolarized $^{129}$Xe | lung function | microvasculature

## ABSTRACT

**Purpose:** To evaluate the feasibility of measuring gas exchange between the alveolar-capillary membrane and red blood cells (RBCs) using hyperpolarized $^{129}$Xe magnetic resonance, and to assess its potential for detecting disease-related changes in an animal model.

**Methods:** Experiments were performed on eight rats with bleomycin-induced pulmonary fibrosis and eight healthy controls. RBCs chemical shift saturation recovery (rCSSR) and equivalent chemical shift saturation recovery (eCSSR) sequences were developed to estimate the gas exchange time constants from alveoli to RBCs ($T_{G\text{-}R}$) and from membrane to RBCs ($T_{M\text{-}R}$). Group comparisons were performed, and correlations between rCSSR-derived parameters and pulmonary function tests (PFTs) and quantitative histology were also assessed. Statistical significance was defined as $p < 0.05$.

**Results:** $T_{M\text{-}R}$ and $T_{G\text{-}R}$ measured with rCSSR (denoted as $T_{M\text{-}R\text{-}R}$ and $T_{G\text{-}R\text{-}R}$, respectively) were higher in the fibrosis group ($8.74 \pm 1.26$ and $17.80 \pm 3.08$ ms, respectively) compared to controls ($7.02 \pm 0.58$ and $13.89 \pm 1.58$ ms; $p < 0.01$). For the $T_{M\text{-}R}$ and $T_{G\text{-}R}$ derived from eCSSR (denoted as $T_{M\text{-}R\text{-}E}$ and $T_{G\text{-}R\text{-}E}$, respectively), only $T_{G\text{-}R\text{-}E}$ showed a significant difference. Additionally, $T_{M\text{-}R\text{-}R}$ demonstrated strong correlations with forced vital capacity, quasi-static compliance from PFTs, and alveolar septal thickness measured by histology.

**Conclusion:** We proposed a $^{129}$Xe MR-based approach for quantifying gas exchange from the alveolar-capillary membrane to RBCs. This technique shows promise as a sensitive, non-invasive tool for detecting pulmonary gas exchange impairment.

## 1 | Introduction

Pulmonary fibrosis is characterized by excessive accumulation of extracellular matrix and remodeling of lung architecture [1]. Idiopathic pulmonary fibrosis (IPF), the most common and severe form, is associated with a median survival of only 3–5 years following diagnosis [2]. Clinically, patients with IPF typically exhibit decreased lung compliance, reduced lung capacity [3], and impaired gas exchange due to pathological thickening of the alveolar-capillary membrane [3, 4]. The pulmonary vasculature

Ming Zhang and Haidong Li contributed equally to this work.

© 2026 International Society for Magnetic Resonance in Medicine.

is essential for gas exchange and plays a key role in lung development, repairment, and regeneration [5]. In patients with IPF, the pulmonary vasculature undergoes aberrant remodeling [5, 6], which may lead to pulmonary arterial and systemic hypertension [7, 8].

Several imaging modalities are used to assess the pulmonary vasculature, including intravascular ultrasound (IVUS) [9], positron emission tomography (PET) [10], computed tomography (CT) [11], and MRI [12]. IVUS enables visualization of vessel wall morphology and pulsation but is invasiveness [13]. PET and CT are widely used for diagnosing pulmonary embolism and atherosclerosis [14, 15]. Nevertheless, their reliance on radioactive tracers or iodine-based contrast agents limits broader application. MRI enables noninvasive assessment of structural and flow-related information, but is challenged by low proton density and susceptibility artifacts in the lung [16]. Importantly, none of these techniques can evaluate capillary networks at the gas exchange interface.

Hyperpolarized $^{129}$Xe gas MRI has been widely utilized in pulmonary imaging [17–20], and the technique has been approved for clinical use in both China and the United States [21, 22]. This modality enables visualization of pulmonary gas distribution and assessments of regional ventilation and alveolar microstructure [23–27]. Xenon can dissolve into the alveolar-capillary membrane and red blood cells (RBCs) within the capillary bed (referred to as dissolved-phase $^{129}$Xe). Due to its high chemical shift sensitivity, these dissolved compartments generate distinct MR signals [28–32]. Numerous studies have used $^{129}$Xe MR to investigate gas exchange from the alveoli to the membrane and RBCs [33–37]. However, the specific gas transfer process from the membrane to RBCs remains poorly characterized. Investigating this intermediate step may offer valuable insights into pulmonary microvascular morphology and function, which could enhance our understanding of microcirculatory impairment in lung pathology.

In this study, we introduce a novel method to evaluate pulmonary capillary function by quantifying xenon exchange between the alveolar-capillary membrane and RBCs. The exchange time constant between membrane and RBCs was extracted from healthy and fibrotic rats and compared to values from an equivalent chemical shift saturation recovery (eCSSR) sequence. Pulmonary function tests (PFTs) and quantitative histological analyses were also performed. The exchange time constants obtained via hyperpolarized $^{129}$Xe MR were correlated with PFT and histological results, providing a comprehensive assessment of pulmonary capillary function.

## 2 | Methods

### 2.1 | Pulse Sequence Design

The central concept for assessing gas exchange between the pulmonary membrane and RBCs is to selectively saturate the $^{129}$Xe signal in the RBCs after the dissolved-phase $^{129}$Xe reaches a steady state. Immediately following this selective saturation, it is assumed that hyperpolarized $^{129}$Xe signal in the RBCs originates exclusively from the membrane. To implement this strategy, we developed a pulse sequence termed RBCs chemical shift saturation recovery (rCSSR), as illustrated in Figure 1A.

In the rCSSR sequence, a low flip-angle Gaussian pulse was applied to acquire the alveolar gas-phase $^{129}$Xe signal ($S_{Gas}$), which was used to normalize the RBCs signal and correct for polarization decay across sequence repetitions. A 400 ms delay is then introduced to allow complete recovery of the dissolved-phase $^{129}$Xe signal in rats, followed by a selective minimum-phase Shinnar–Le Roux (SLR) pulse (SLR2) to selectively saturate the $^{129}$Xe signal in RBCs. Subsequently, after a variable exchange time ($\tau$), the dissolved-phase $^{129}$Xe signal is excited to quantify the signals in the membrane compartment ($S_{Mem}$), and RBCs ($S_{RBCs}$). Additionally, replacing the SLR2 pulse with SLR1

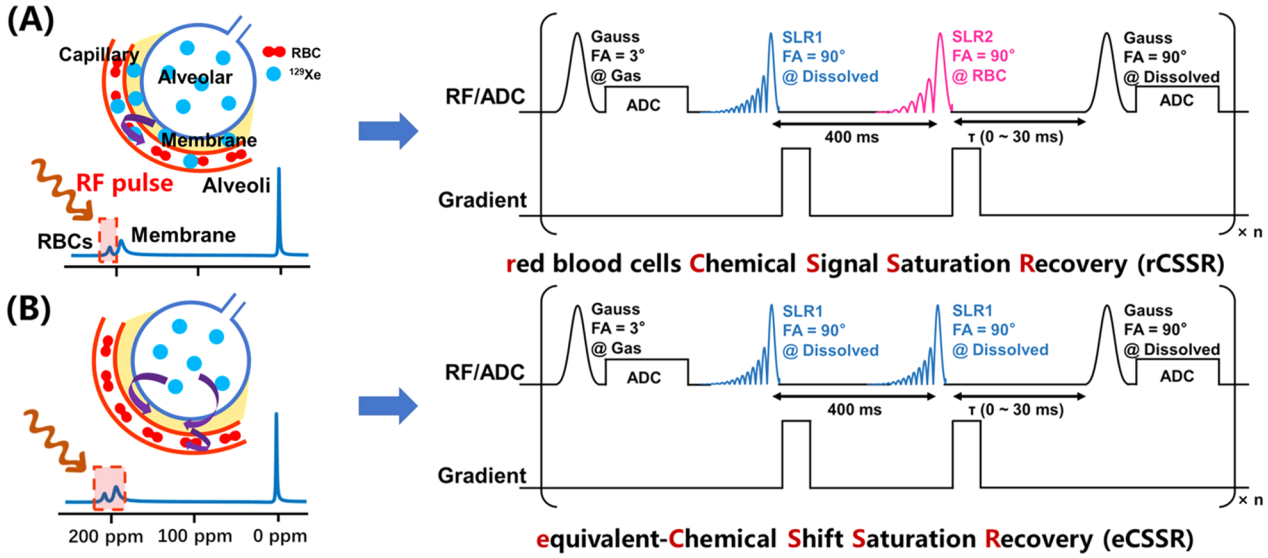


**FIGURE 1** | Pulse sequences designed in this study. (A) RBCs chemical shift saturation recovery (rCSSR). (B) Equivalent CSSR sequence (eCSSR). Each sequence was repeated $n$ times, with the exchange time ($\tau$) varying as a function of $n$. ADC, analog-to-digital converter; FA, flip angle; RBCs, red blood cells; RF, radiofrequency; SLR, Shinnar–Le Roux algorithm.



15222594, 0, Downloaded from https://onlinelibrary.wiley.com/doi/10.1002/mrm.70279 by Huazhong University Of Science, Wiley Online Library on [01/02/2026]. See the Terms and Conditions (https://onlinelibrary.wiley.com/terms-and-conditions) on Wiley Online Library for rules of use; OA articles are governed by the applicable Creative Commons License

yields a functionally eCSSR sequence, here referred to as eCSSR (Figure 1B).

For both rCSSR and eCSSR, the measured $S_{Gas}$, $S_{Mem}$, and $S_{RBCs}$ were fitted according to Equations (1) and (2), derived from the model proposed by Månsson et al. [38]:

$$\frac{S_{RBCs}(t)}{S_{Gas}(t)} = A_{G-R} \times \left(1 - e^{-t/T_{G-R}}\right) + C_{G-R} \quad (1)$$

$$\frac{S_{RBCs}(t)}{S_{Mem}(t)} = A_{M-R} \times \left(1 - e^{-t/T_{M-R}}\right) + C_{M-R} \quad (2)$$

wherein $T_{G\text{-}R}$ and $T_{M\text{-}R}$ represent the exchange time constants for $^{129}$Xe from the alveoli and membrane to the RBCs, respectively. Parameters $A_{G\text{-}R}$ and $A_{M\text{-}R}$ are scaling factors, and $C_{G\text{-}R}$ and $C_{M\text{-}R}$ are fitting constants. $T_{G\text{-}R}$ and $T_{M\text{-}R}$ measured with rCSSR are denoted as $T_{G\text{-}R\text{-}R}$ and $T_{M\text{-}R\text{-}R}$, while those derived from eCSSR are denoted as $T_{G\text{-}R\text{-}E}$ and $T_{M\text{-}R\text{-}E}$. Because the variable delay time ($\tau$) was restricted to 30 ms, the contribution from blood flow was considered negligible; hence, the linear term was omitted in the fitting model.

## 2.2 | Animal Preparation

All animal procedures were approved by the Institutional Review Board at Innovation Academy for Precision Measurement Science and Technology, Chinese Academy of Sciences, in compliance with the laws governing animal experimentation. Sixteen male Sprague–Dawley rats (200 ± 20 g) were randomly assigned to control or fibrosis groups ($n = 8$ per group) after acclimatization. Pulmonary fibrosis was induced by intratracheal instillation of bleomycin (3 U/kg in 0.4 mL saline; Shanghai Macklin Biochemical Co. Ltd., Shanghai, China) [17], while controls received 0.4 mL normal saline. Anesthesia was induced with 5% isoflurane and maintained at 2%. All measurements were performed between Days 21 and 22 post-treatment [39].

## 2.3 | Pulmonary Function Tests (PFTs)

PFTs were performed using a Forced Maneuvers system (CRFM 100, EMMS, UK). Rats were anesthetized with sodium pentobarbital (30 mg/kg, intraperitoneal injection) and underwent tracheostomy [40]. A 14-G endotracheal tube was inserted into the trachea and secured with surgical thread, then connected to the plethysmograph. Measurements of forced vital capacity (FVC), functional residual capacity (FRC), total lung capacity (TLC), and quasi-static lung compliance ($C_{qs}$) were obtained within 5 min.

## 2.4 | $^{129}$Xe Polarization and Delivery

Isotopically enriched xenon gas (86% $^{129}$Xe) was polarized via spin-exchange optical pumping using a commercial polarizer system (verImagin Healthcare, Wuhan, China). A total of 200 mL of hyperpolarized $^{129}$Xe gas was cryogenically accumulated in 15 min and then thawed into a Tedlar bag [41] with approximately 40% polarization.

For $^{129}$Xe MR examinations, xenon and oxygen gas were alternately delivered to the rat lungs using a homebuilt MR-compatible hyperpolarized gas delivery system [40, 41], controlled by LabVIEW. During the experiment, the lung pressure of the rats was maintained below 15 cm $H_2O$.

## 2.5 | $^{129}$Xe MR Experiments

Following PFTs, each rat underwent $^{129}$Xe MR using a 7.0T animal MRI scanner (Bruker Biospec 70/20 USR, Germany) equipped with a home-built, dual-tuned birdcage coil. Anesthesia was maintained with 2% isoflurane.

Both rCSSR and eCSSR sequences were performed on each rat. In the rCSSR sequence, the first and fourth RF pulses were Gaussian pulses (0.3 ms, flip angles of 3° and 90°, respectively), aiming at gas-phase and dissolved-phase $^{129}$Xe, respectively. Minimal-phase SLR RF pulses SLR1 (2 ms, 7.5 kHz bandwidth) and SLR2 (4 ms, 2.25 kHz bandwidth) were designed with 0.01% passband and stopband ripple. The off-resonance excitation on gas-phase $^{129}$Xe of SLR1 and SLR2 were 0.4° and 0.09°, respectively. SLR2 was optimized for selective excitation of $^{129}$Xe signals in RBCs [34, 42]. The simulated and experimentally measured excitation profiles of the SLR1 and SLR2 are shown in Figure S1. Fourteen dynamic spectra were acquired with exchange times ($\tau$) ranging from 1 to 30 ms (1, 2, 3, 4, 5, 6, 7, 8, 9, 10, 15, 20, 25, and 30 ms), with a bandwidth of 25 kHz and 1024 sampling points. In the eCSSR sequence, all parameters were identical to those of the rCSSR sequence, except that the SLR2 was replaced with SLR1.

Each rat received six pre-breaths of hyperpolarized $^{129}$Xe prior to data acquisition to purge residual oxygen and enhance spectral SNR [40]. Three repetitions of rCSSR and eCSSR were performed on each rat. The total breath-hold time for each sequence was 7.5 s.

## 2.6 | Data Processing

All MR data were processed using MATLAB software (MathWorks, Natick, MA). Considering the short $T_2$* of dissolved-phase $^{129}$Xe, prolonged acquisition times would introduce unnecessary noise into the spectrum. Therefore, for each FID, the first 512 sampling points were extracted and then zero-filled to 1024 points prior to Fourier transformation, thereby reducing noise contributions while maintaining sufficient spectral resolution. The signal amplitudes of dissolved ($S_{Mem}$ and $S_{RBCs}$) and gaseous xenon ($S_{Gas}$) were extracted by fitting the MR data to the Lorentzian shape function [43]. Exchange time constants $T_{M\text{-}R}$ and $T_{G\text{-}R}$ for both rCSSR (denoted as $T_{M\text{-}R\text{-}R}$ and $T_{G\text{-}R\text{-}R}$) and eCSSR (denoted as $T_{M\text{-}R\text{-}E}$ and $T_{G\text{-}R\text{-}E}$) were obtained by fitting the signal amplitudes to Equations (1) and (2), respectively.

## 2.7 | Quantitative Histology

After $^{129}$Xe MR, rats were sacrificed and lungs were inflated with 4% paraformaldehyde at 25 cm $H_2O$ pressure for 2 h and subsequently fixed for ≥ 48 h. Lungs were paraffin-embedded, sectioned (5 μm thickness), and stained with hematoxylin and eosin (H&E). Airway-free microscopy images (Nikon Eclipse Ts 100)



15222594, 0, Downloaded from https://onlinelibrary.wiley.com/doi/10.1002/mrm.70279 by Huazhong University Of Science, Wiley Online Library on [01/02/2026]. See the Terms and Conditions (https://onlinelibrary.wiley.com/terms-and-conditions) on Wiley Online Library for rules of use; OA articles are governed by the applicable Creative Commons License

were analyzed with custom MATLAB program. Septal wall thickness was calculated as the average truncated length overlaid with a standard test grid [44, 45].

### 2.8 | Statistical Analysis

Statistical analyses were performed using the SPSS Statistics 20 (IBM, Armonk, NY, USA). Data normality was confirmed with the Shapiro–Wilk test. Results are represented as mean ± standard deviation (SD). Unpaired *t*-tests were used for group comparisons. Pearson correlation coefficients ($r$) were calculated to assess the relationships between exchange time constants (from rCSSR and eCSSR) and PFTs measurements (FVC and $C_{qs}$) or septal wall thickness from quantitative histology. A $p$-value $< 0.05$ was considered statistically significant.

## 3 | Results

### 3.1 | Hyperpolarized $^{129}$Xe MR

Representative $^{129}$Xe spectra acquired from a control rat using rCSSR and eCSSR sequences are shown in Figure 2A,B. Due to the fixed 400 ms delay in both sequences—during which the dissolved-phase $^{129}$Xe signal reaches equilibrium and does not change rapidly over time—the resulting TR exceeds 500 ms and the gaseous signal decays rapidly with repeated sequence acquisition. Representative $^{129}$Xe spectra at an exchange time of 10 ms from the control and fibrosis rats are shown in zoomed-in views. In the rCSSR, the measured $S_{Mem}/S_{Gas}$ ratio is higher than that measured in eCSSR. Specifically, at an exchange time of 10 ms, the $S_{Mem}/S_{Gas}$ ratios for the control group were $0.0103 \pm 0.0012$ for eCSSR and $0.0158 \pm 0.0017$ for rCSSR ($p < 0.001$), and for the fibrosis group were $0.0088 \pm 0.0018$ for eCSSR and $0.0150 \pm 0.0028$ for rCSSR ($p < 0.001$). Moreover, in both rCSSR and eCSSR, the $^{129}$Xe signal in RBCs is reduced in the fibrosis group compared to the control group. Specifically, at an exchange time of 10 ms, the measured $S_{RBCs}/S_{Mem}$ ratio in the fibrosis group was reduced by 1.3-fold compared to the control group in the rCSSR sequence (control: $0.47 \pm 0.06$, fibrosis: $0.36 \pm 0.06$, $p = 0.004$) and by 1.2-fold in the eCSSR sequence (control: $0.46 \pm 0.05$, fibrosis: $0.38 \pm 0.05$, $p = 0.008$).

Decreased signal ratios were observed in the fibrosis rat compared with the control rat at most exchange times (Figure 2C). Additionally, the rCSSR-derived $S_{RBCs}/S_{Mem}$ and $S_{RBCs}/S_{Gas}$

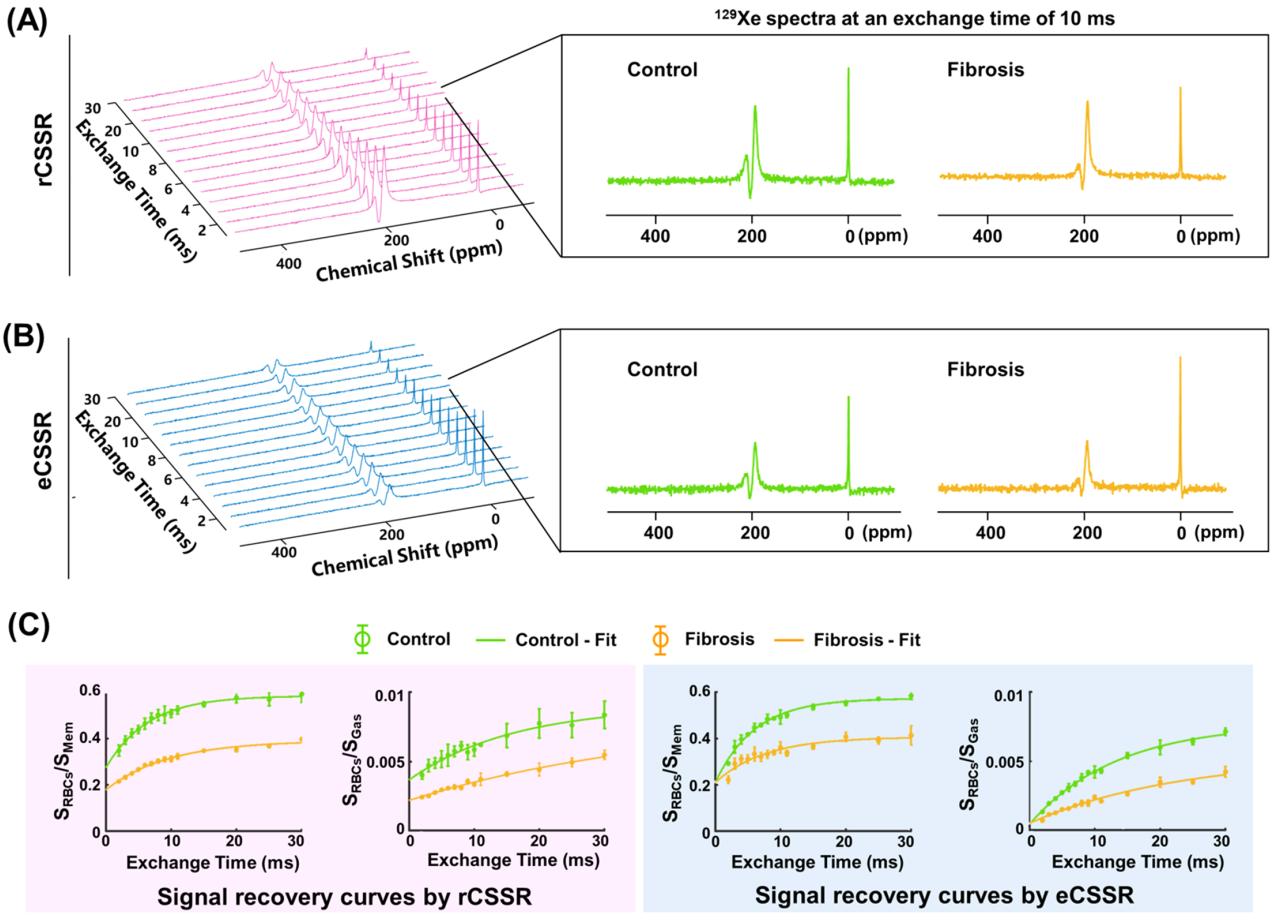


**FIGURE 2** | Dynamics of hyperpolarized $^{129}$Xe magnetic resonance spectroscopy in a representative control rat, obtained from (A) rCSSR and (B) eCSSR sequences, respectively. Representative $^{129}$Xe spectra with an exchange time of 10 ms from the control and fibrosis groups are shown in zoomed-in views, where the fibrosis group shows a decreased $^{129}$Xe signal in RBCs compared to the control group. (C) Representative recovery curves of $S_{RBCs}/S_{Mem}$ and normalized $S_{RBCs}/S_{Gas}$ from the rCSSR and eCSSR. Each point on the curve represents the average of three independent experiments. In each plot, the recovery curve for the fibrosis group lies below that of the control group. In rCSSR, the $S_{RBCs}/S_{Mem}$ in the fibrosis group shows a slower recovery than in the control group. eCSSR, equivalent chemical shift saturation recovery; rCSSR, red blood cells chemical shift saturation recovery.



15222594, 0, Downloaded from https://onlinelibrary.wiley.com/doi/10.1002/mrm.70279 by Huazhong University Of Science, Wiley Online Library on [01/02/2026]. See the Terms and Conditions (https://onlinelibrary.wiley.com/terms-and-conditions) on Wiley Online Library for rules of use; OA articles are governed by the applicable Creative Commons License

ratios in the fibrosis group exhibited a significantly slower recovery compared to those in the control group. A similar trend was also observed in the normalized $S_{RBCs}/S_{Gas}$ obtained from eCSSR. Quantitatively, the $T_{M\text{-}R\text{-}R}$ in the fibrosis group ($8.74 \pm 1.26$ ms) was significantly higher than that in the control group ($7.02 \pm 0.58$ ms, $p = 0.006$). Both $T_{G\text{-}R\text{-}R}$ and $T_{G\text{-}R\text{-}E}$ were also elevated in the fibrosis group. Specifically, $T_{G\text{-}R\text{-}R}$ was $13.89 \pm 1.58$ ms in the control group and $17.80 \pm 3.08$ ms in the fibrosis group ($p = 0.006$), while $T_{G\text{-}R\text{-}E}$ was $16.56 \pm 2.01$ and $22.42 \pm 5.13$ ms in the control and fibrosis groups, respectively ($p = 0.009$) (Table 1). Changes in the $S_{Mem}/S_{Gas}$ ratio as a function of exchange time were also evaluated for both eCSSR and rCSSR (Figure S2). In eCSSR, $S_{Mem}/S_{Gas}$ increases with exchange time, whereas in rCSSR, it exhibits an initial dip at very short exchange times, probably caused by the transfer of magnetization from the membrane to the RBC compartment.

**TABLE 1** | Summary of results from $^{129}$Xe MR and PFTs.

| | Control | Fibrosis | *p* |
|---|---|---|---|
| rCSSR | | | |
| $T_{M\text{-}R\text{-}R}$ (ms) | $7.02 \pm 0.58$ | $8.74 \pm 1.26$ | 0.006* |
| $T_{G\text{-}R\text{-}R}$ (ms) | $13.89 \pm 1.58$ | $17.80 \pm 3.08$ | 0.009* |
| eCSSR | | | |
| $T_{M\text{-}R\text{-}E}$ (ms) | $6.45 \pm 0.61$ | $7.00 \pm 0.68$ | 0.109 |
| $T_{G\text{-}R\text{-}E}$ (ms) | $16.56 \pm 2.01$ | $22.42 \pm 5.13$ | 0.009* |
| PFTs | | | |
| FVC (mL) | $11.12 \pm 0.77$ | $6.00 \pm 2.10$ | < 0.001* |
| FRC (mL) | $3.40 \pm 0.45$ | $4.14 \pm 0.93$ | 0.069 |
| TLC (mL) | $13.22 \pm 1.33$ | $8.75 \pm 2.04$ | < 0.001* |
| $C_{qs}$ (mL/$H_2O$) | $0.84 \pm 0.14$ | $0.35 \pm 0.10$ | < 0.001* |

*Note:* Data are presented as mean ± standard deviation.

Abbreviations: $C_{qs}$, quasi-static lung compliance; eCSSR, equivalent chemical shift saturation recovery; FRC, functional residual capacity; FVC, forced vital capacity; rCSSR, red blood cells chemical shift saturation recovery; $T_{G\text{-}R\text{-}R}$ and $T_{G\text{-}R\text{-}E}$, $^{129}$Xe exchange time constants from alveoli to red blood cells, derived from rCSSR and eCSSR, respectively; TLC, total lung capacity; $T_{M\text{-}R\text{-}R}$ and $T_{M\text{-}R\text{-}E}$, $^{129}$Xe exchange time constants from membrane to red blood cells, derived from rCSSR and eCSSR, respectively.

*$p < 0.05$, unpaired *t*-test.

## 3.2 | Pulmonary Function Tests

Compared to the control group, the fibrosis group showed significantly reduced pulmonary function. FVC, TLC, and $C_{qs}$ were significantly lower in the fibrosis group ($6.00 \pm 2.10$ mL, $8.75 \pm 2.04$ mL, and $0.35 \pm 0.10$ mL/$H_2O$, respectively) compared to the control group ($11.12 \pm 0.77$ mL, $13.22 \pm 1.33$ mL, and $0.84 \pm 0.14$ mL/$H_2O$, respectively; Table 1, $p < 0.05$).

## 3.3 | Histological Observations

Pulmonary H&E-stained sections showed significant thickening of the alveolar wall in the fibrosis group compared to the control group (Figure 3). The septal wall thickness in the fibrosis group was significantly higher than in the control group (Control: $4.64 \pm 0.47$ μm, Fibrosis: $7.87 \pm 1.47$ μm, $p = 0.001$).

## 3.4 | Correlation of the Exchange Time Constant With PFTs and Quantitative Histology

Figure 4 shows the correlation of $T_{M\text{-}R\text{-}R}$, $T_{G\text{-}R\text{-}R}$, $T_{M\text{-}R\text{-}E}$, and $T_{G\text{-}R\text{-}E}$ with FVC and $C_{qs}$ measured with PFTs and septal wall thickness measured with quantitative histology, respectively. $T_{M\text{-}R\text{-}R}$ showed a significant negative correlation with FVC ($r = -0.813$, $p < 0.001$) and $C_{qs}$ ($r = -0.809$, $p < 0.001$), and a positive correlation with septal wall thickness ($r = 0.744$, $p = 0.001$).

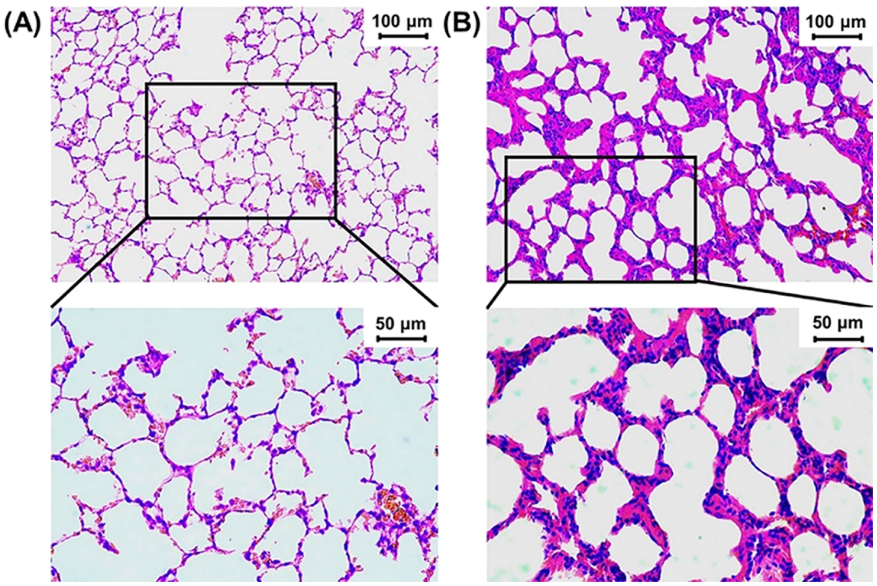


**FIGURE 3** | Representative hematoxylin and eosin (H&E) stained lung sections from (A) control and (B) fibrosis rats. The alveolar septal wall thickness in the fibrosis rat lung shows a significant increase compared to the control rat (top: Scale bar = 100 μm, bottom: Scale bar = 50 μm).



15222594, 0, Downloaded from https://onlinelibrary.wiley.com/doi/10.1002/mrm.70279 by Huazhong University Of Science, Wiley Online Library on [01/02/2026]. See the Terms and Conditions (https://onlinelibrary.wiley.com/terms-and-conditions) on Wiley Online Library for rules of use; OA articles are governed by the applicable Creative Commons License

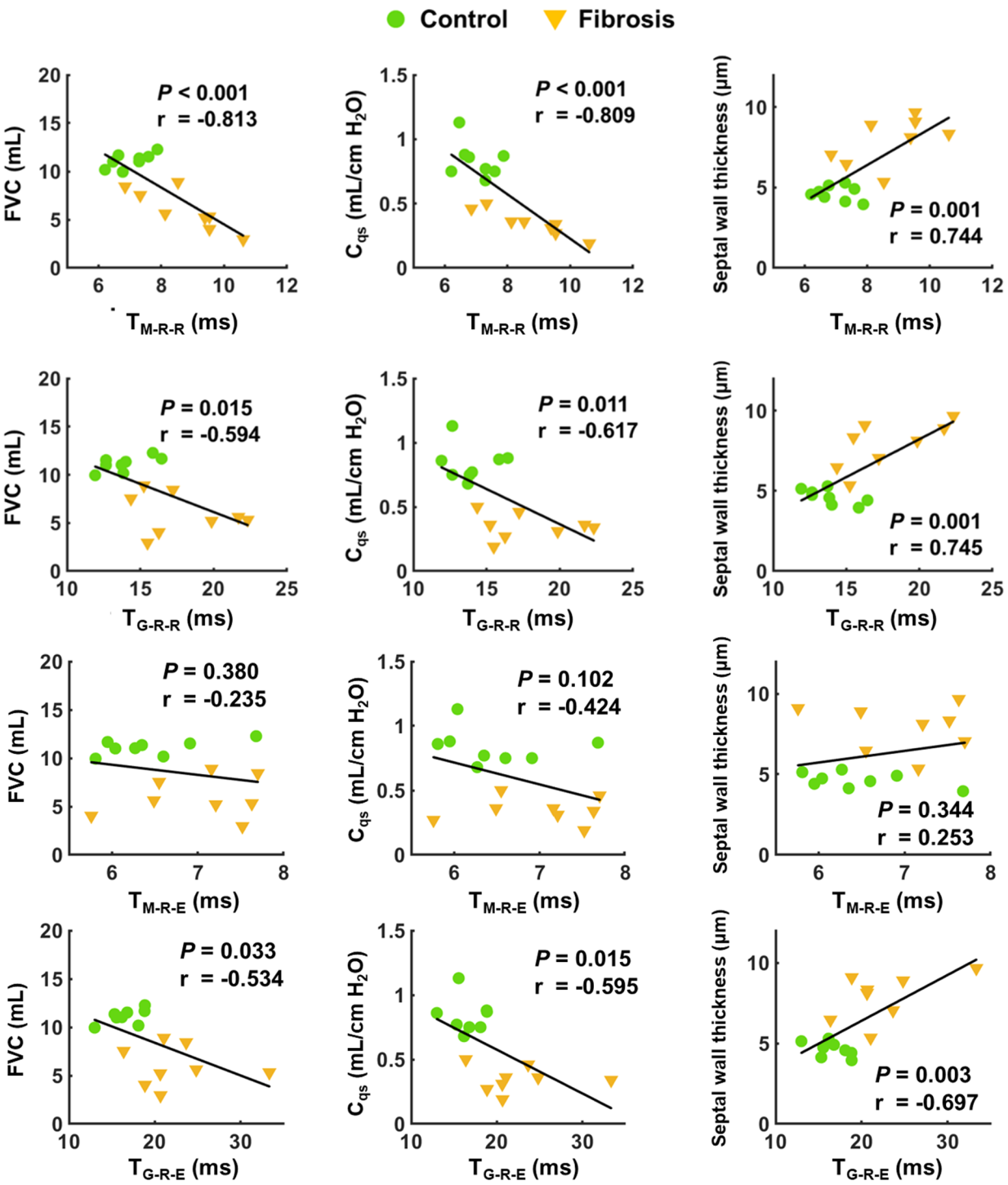


**FIGURE 4** | Correlation of the exchange time constant between the membrane and RBCs ($T_{M\text{-}R\text{-}R}$, $T_{M\text{-}R\text{-}E}$) and between the alveoli and RBCs ($T_{G\text{-}R\text{-}R}$, $T_{G\text{-}R\text{-}E}$) measured by rCSSR and eCSSR, with results from PFTs and quantitative histology. $C_{qs}$, quasi-static lung compliance; eCSSR, equivalent chemical shift saturation recovery; FVC, forced vital capacity; PFTs, pulmonary function tests; RBCs, red blood cells; rCSSR, RBCs chemical shift saturation recovery.

## 4 | Discussion

In this study, a novel method for measuring the pulmonary capillary function using hyperpolarized xenon MR, specifically rCSSR, was proposed. The gas exchange time constant from the membrane to RBCs was measured and found to be elevated in the fibrosis group compared to the control group, and it showed a strong correlation with PFTs results and quantitative histology. These findings suggest that the proposed method has the potential for sensitively detecting gas exchange abnormalities from the membrane to RBCs in pulmonary fibrosis.

In this study, two new exchange time constants were proposed: $T_{M\text{-}R}$ and $T_{G\text{-}R}$, representing the time required for $^{129}$Xe gas



15222594, 0, Downloaded from https://onlinelibrary.wiley.com/doi/10.1002/mrm.70279 by Huazhong University Of Science, Wiley Online Library on [01/02/2026]. See the Terms and Conditions (https://onlinelibrary.wiley.com/terms-and-conditions) on Wiley Online Library for rules of use; OA articles are governed by the applicable Creative Commons License

exchange from the membrane to RBCs and from the alveoli to RBCs, respectively. Both $T_{G\text{-}R}$ and $T_{M\text{-}R}$ measured with rCSSR ($T_{G\text{-}R\text{-}R}$ and $T_{M\text{-}R\text{-}R}$) increased significantly in the fibrosis group. The observed change in $T_{M\text{-}R\text{-}R}$ may be attributed to pulmonary capillary remodeling associated with fibrosis [46, 47], which may lead to thickening of the capillary wall [48, 49] and consequently prolong the time required for xenon to bind with hemoglobin within RBCs. The change in $T_{G\text{-}R\text{-}R}$ may result from thickened alveolar tissues in fibrotic lungs [50], which hinder the xenon diffusion from alveoli to capillaries [4, 51, 52]. These results showed good agreement with the results of PFTs and histological sections.

To investigate the gas exchange function between membrane and capillary, this study introduces the rCSSR sequence. Traditionally, gas exchange assessment has relied on the CSSR technique [40, 41]. In CSSR, saturation is applied to the entire dissolved-phase $^{129}$Xe signal, while alveolar $^{129}$Xe serves as a stable reservoir, allowing quantification of xenon transfer into both the membrane and RBCs compartments. In contrast, the rCSSR sequence differs from CSSR in two principal ways. First, signal saturation is only applied to the $^{129}$Xe signal in RBCs. Second, a 400 ms preparation delay is introduced for the rCSSR sequence to establish a stable $^{129}$Xe signal source within the membrane. Previous studies have shown that the dissolved-phase $^{129}$Xe signal reaches a relatively steady state at longer exchange times in rat lungs [40, 41]. This design ensures that, immediately after saturation, the $^{129}$Xe in RBCs primarily originates from the membrane.

We proposed an eCSSR sequence by modifying the saturation target. Using this sequence, $T_{G\text{-}R}$ and $T_{M\text{-}R}$ were obtained and denoted as $T_{G\text{-}R\text{-}E}$ and $T_{M\text{-}R\text{-}E}$, respectively. In both eCSSR and rCSSR, $T_{G\text{-}R}$ exceeded $T_{M\text{-}R}$, consistent with the process of $^{129}$Xe uptake [53]: after inhalation, $^{129}$Xe diffuses from alveoli to membrane, generating $S_{Mem}$, then into the capillary blood, where it binds to hemoglobin within RBCs, generating $S_{RBCs}$. Thus, the xenon transfer time from alveoli to RBCs ($T_{G\text{-}R}$) is inherently longer than that from membrane to RBCs ($T_{M\text{-}R}$). Notably, $T_{G\text{-}R\text{-}E}$ was higher than $T_{G\text{-}R\text{-}R}$, likely reflecting the distinct magnetization recovery mechanisms of the two sequences. In rCSSR, only the RBCs signal is saturated, allowing rapid replenishment from the membrane; whereas in eCSSR, both membrane and RBCs are saturated, requiring xenon to traverse the entire diffusion pathway before recovery.

As expected, the fibrosis group exhibited lower FVC, TLC, and $C_{qs}$, consistent with prior reports in bleomycin-induced pulmonary fibrosis models [54, 55]. These changes reflect decreased lung compliance and volume, likely caused by extracellular matrix deposition and myofibroblast proliferation following bleomycin instillation [39]. This was corroborated by histological evidence of thickened alveolar septa and fibrotic tissue, indicative of stiffer lung parenchyma.

### 4.1 | Limitations

There are several aspects in our study that could be optimized. First, although a 400 ms delay ensures equilibrium in the membrane $^{129}$Xe signal, it may introduce contamination from the heart and downstream regions. The delay should be optimized to maintain a stable membrane signal while confining the blood signal within the pulmonary capillary bed. In addition, to improve $T_{M\text{-}R\text{-}R}$ estimation, future studies should employ a more optimized RBCs saturation scheme and incorporate models accounting for blood flow, reducing the dependence of fitted parameters on the maximum exchange time. Moreover, our study can be extended in the following aspects. Although $T_{M\text{-}R\text{-}R}$ may serve as a biomarker of pulmonary capillary remodeling, a detailed theoretical model is needed to extract specific structural parameters of the capillaries. Additionally, while the proposed method provides a global measurement of gas exchange between the membrane and RBCs, future work should incorporate dissolved-phase $^{129}$Xe imaging for spatially resolved evaluations. Finally, besides capillary changes, alterations in RBCs may influence gas exchange; therefore, RBCs-related disorders, such as sickle cell anemia, should be considered.

## 5 | Conclusion

In this study, a method using hyperpolarized $^{129}$Xe MR to assess gas exchange between the alveolar-capillary membrane and RBCs was proposed. The feasibility of such method for evaluating capillary alterations in a pulmonary fibrosis animal model was demonstrated. The gas exchange time constant between the membrane and RBCs was significantly higher in fibrosis than controls. These findings suggest that the proposed method may serve as a sensitive tool for detecting pulmonary gas exchange and support future clinical research in the diagnosis and monitoring of pulmonary fibrosis.


#### Acknowledgments

Financial supports by the National Natural Science Foundation of China, the Strategic Priority Research Program of the Chinese Academy of Sciences, the Key Research Program of Frontier Sciences, CAS, the Scientific Instrument Developing Project of the Chinese Academy of Sciences, the Major Program (JD) of Hubei Province and the Hubei Province Outstanding Youth Fund, and the Hubei Province Science and Technology Innovation Talent Program are gratefully acknowledged.

#### Funding

This work was supported by the National Natural Science Foundation of China (82441015, 82127802, 82372150, T2522037, 82502586), the Strategic Priority Research Program of the Chinese Academy of Sciences (XDC0170000), the Key Research Program of Frontier Sciences, CAS (ZDBS-LY-JSC004), the Scientific Instrument Developing Project of the Chinese Academy of Sciences (PTYQ2024TD0001), the Major Program (JD) of Hubei Province (2023BAA021) and the Hubei Province Outstanding Youth Fund (2023AFA112), and the Hubei Province Science and Technology Innovation Talent Program (2024DJA001).


#### Conflicts of Interest

The authors declare no conflicts of interest.

#### Data Availability Statement

The data that support the findings of this study are available following reasonable requests to the corresponding author.



15222594, 0, Downloaded from https://onlinelibrary.wiley.com/doi/10.1002/mrm.70279 by Huazhong University Of Science, Wiley Online Library on [01/02/2026]. See the Terms and Conditions (https://onlinelibrary.wiley.com/terms-and-conditions) on Wiley Online Library for rules of use; OA articles are governed by the applicable Creative Commons License

## References


1. N. W. Todd, I. G. Luzina, and S. P. Atamas, "Molecular and Cellular Mechanisms of Pulmonary Fibrosis," *Fibrogenesis & Tissue Repair* 5 (2012): 1–24.

2. J. Behr, A. Prasse, H. Wirtz, et al., "Survival and Course of Lung Function in the Presence or Absence of Antifibrotic Treatment in Patients With Idiopathic Pulmonary Fibrosis: Long-Term Results of the INSIGHTS-IPF Registry," *European Respiratory Journal* 56, no. 2 (2020): 1902279.

3. L. Plantier, A. Cazes, A.-T. Dinh-Xuan, C. Bancal, S. Marchand-Adam, and B. Crestani, "Physiology of the Lung in Idiopathic Pulmonary Fibrosis," *European Respiratory Review* 27, no. 147 (2018): 170062.

4. J. M. Wang, S. H. Robertson, Z. Y. Wang, et al., "Using Hyperpolarized Xe-129 MRI to Quantify Regional Gas Transfer in Idiopathic Pulmonary Fibrosis," *Thorax* 73, no. 1 (2018): 21–28.

5. N. Caporarello and G. Ligresti, "Vascular Contribution to Lung Repair and Fibrosis," *American Journal of Respiratory Cell and Molecular Biology* 69, no. 2 (2023): 135–146.

6. C. Hanumegowda, L. Farkas, and M. Kolb, "Angiogenesis in Pulmonary Fibrosis: Too Much or Not Enough?," *Chest* 142, no. 1 (2012): 200–207.

7. H. F. Nadrous, P. A. Pellikka, M. J. Krowka, et al., "The Impact of Pulmonary Hypertension on Survival in Patients With Idiopathic Pulmonary Fibrosis," *Chest* 128, no. 6 (2005): 616S–617S.

8. C. J. Lettieri, S. D. Nathan, S. D. Barnett, S. Ahmad, and A. F. Shorr, "Prevalence and Outcomes of Pulmonary Arterial Hypertension in Advanced Idiopathic Pulmonary Fibrosis," *Chest* 129, no. 3 (2006): 746–752.

9. E. Bressollette, J. Dupuis, R. Bonan, S. Doucet, P. Cernacek, and J.-C. Tardif, "Intravascular Ultrasound Assessment of Pulmonary Vascular Disease in Patients With Pulmonary Hypertension," *Chest* 120, no. 3 (2001): 809–815.

10. G. Marsboom, C. Wietholt, C. R. Haney, et al., "Lung 18F-Fluorodeoxyglucose Positron Emission Tomography for Diagnosis and Monitoring of Pulmonary Arterial Hypertension," *American Journal of Respiratory and Critical Care Medicine* 185, no. 6 (2012): 670–679.

11. P. Rajiah, Y. Tanabe, S. Partovi, and A. Moore, "State of the Art: Utility of Multi-Energy CT in the Evaluation of Pulmonary Vasculature," *International Journal of Cardiovascular Imaging* 35 (2019): 1509–1524.

12. M. Aziz, M. Krishnam, A. J. Madhuranthakam, and P. Rajiah, "Update on MR Imaging of the Pulmonary Vasculature," *International Journal of Cardiovascular Imaging* 35 (2019): 1483–1497.

13. K. M. Coy, G. Maurer, and R. J. Siegel, "Intravascular Ultrasound Imaging: A Current Perspective," *Journal of the American College of Cardiology* 18, no. 7 (1991): 1811–1823.

14. H. Doğan, A. de Roos, J. Geleijins, M. V. Huisman, and L. J. Kroft, "The Role of Computed Tomography in the Diagnosis of Acute and Chronic Pulmonary Embolism," *Diagnostic and Interventional Radiology* 21, no. 4 (2015): 307–316.

15. N. Alie, M. Eldib, Z. A. Fayad, and V. Mani, "Inflammation, Atherosclerosis, and Coronary Artery Disease: PET/CT for the Evaluation of Atherosclerosis and Inflammation," *Clinical Medicine Insights. Cardiology* 8 (2014): CMC.S17063.

16. M. Taso, V. Aramendía-Vidaurreta, E. K. Englund, et al., "Update on State-Of-The-Art for Arterial Spin Labeling (ASL) Human Perfusion Imaging Outside of the Brain," *Magnetic Resonance in Medicine* 89, no. 5 (2023): 1754–1776.

17. M. Zhang, H. Li, Y. Xiao, et al., "Assessment of Global and Regional Lung Compliance in Pulmonary Fibrosis With Hyperpolarized Gas MRI," *Journal of Magnetic Resonance Imaging* 61, no. 3 (2025): 1404–1415.

18. J. M. Wild, F. V. Gleeson, S. Svenningsen, et al., "Review of Hyperpolarized Pulmonary Functional $^{129}$Xe MR for Long-COVID," *Journal of Magnetic Resonance Imaging* 59, no. 4 (2024): 1120–1134.

19. Q. Rao, H. Li, Q. Zhou, et al., "Assessment of Pulmonary Physiological Changes Caused by Aging, Cigarette Smoking, and COPD With Hyperpolarized $^{129}$Xe Magnetic Resonance," *European Radiology* 34 (2024): 7450–7459.

20. Z. Zhang, H. Li, S. Xiao, et al., "Hyperpolarized Gas Imaging in Lung Diseases: Functional and Artificial Intelligence Perspective," *Academic Radiology* 31, no. 10 (2024): 4203–4216.

21. Y. Yang, S. Yue, L. Shen, et al., "Ultrasensitive $^{129}$Xe Magnetic Resonance Imaging: From Clinical Monitoring to Molecular Sensing," *Advanced Science* 12, no. 8 (2025): 2413426.

22. H. Li, H. Li, M. Zhang, et al., "Advancements and Applications of Hyperpolarized Xenon MRI for COPD Assessment in China," *British Journal of Radiology* (2025): tqaf119, https://doi.org/10.1093/bjr/tqaf119.

23. Y. Fang, H. Li, L. Shen, et al., "Rapid Pulmonary $^{129}$Xe Ventilation MRI of Discharged COVID-19 Patients With Zigzag Sampling," *Magnetic Resonance in Medicine* 92, no. 3 (2024): 956–966.

24. H. Li, H. Li, L. Fan, et al., "Dynamic Ventilation Functional MRI of the Lung With Sub-Millimeter Spatial Resolution and Millisecond Temporal Resolution," *Scientific Bulletin* 70, no. 24 (2025): 4142–4145.

25. L. Shen, H. Li, Y. Fang, et al., "Hyperpolarized $^{129}$Xe Diffusion-Weighted MRI of the Lung With 3D Golden-Angle Radial Sampling and Keyhole Reconstruction," *Medical Physics* 52, no. 6 (2025): 4068–4078.

26. H. Li, X. Zhao, Y. Wang, et al., "Damaged Lung Gas Exchange Function of Discharged COVID-19 Patients Detected by Hyperpolarized $^{129}$Xe MRI," *Science Advances* 7, no. 1 (2021): eabc8180.

27. A. S. Bdaiwi, M. M. Willmering, H. Wang, and Z. I. Cleveland, "Diffusion Weighted Hyperpolarized $^{129}$Xe MRI of the Lung With 2D and 3D (FLORET) Spiral," *Magnetic Resonance in Medicine* 89, no. 4 (2023): 1342–1356.

28. X. Liu, H. Li, H. Li, et al., "Measurement of Pulmonary Hematocrit Using Oscillation of Hyperpolarized $^{129}$Xe MR Signals in Blood," *Magnetic Resonance in Medicine* 93, no. 5 (2025): 1886–1895.

29. Y. Friedlander, B. Zanette, A. Lindenmaier, et al., "Chemical Shift of $^{129}$Xe Dissolved in Red Blood Cells: Application to a Rat Model of Bronchopulmonary Dysplasia," *Magnetic Resonance in Medicine* 84, no. 1 (2020): 52–60.

30. P. J. Niedbalski, M. M. Willmering, R. P. Thomen, et al., "A Single-Breath-Hold Protocol for Hyperpolarized $^{129}$Xe Ventilation and Gas Exchange Imaging," *NMR in Biomedicine* 36, no. 8 (2023): e4923.

31. Q. Zeng, Q. Yue, M. Zhang, et al., "Multivariate Metal-Organic Frameworks Enable Chemical Shift-Encoded MRI With Femtomolar Sensitivity for Biological Systems," *Nature Communications* 16, no. 1 (2025): 6832.

32. B. Driehuys, S. Zhang, A. Bechtel, et al., "Design and Implementation of a Multi-Center Trial of $^{129}$Xe Gas Exchange MRI and MRS to Evaluate Longitudinal Progression of COPD," *Journal of Magnetic Resonance Imaging* 62, no. 6 (2025): 1879–1891.

33. M. Zhang, H. Li, H. Li, et al., "Dynamic Evaluation of Acute Lung Injury Using Hyperpolarized $^{129}$Xe Magnetic Resonance," *NMR in Biomedicine* 37, no. 4 (2024): e5078.

34. H. Li, H. Li, M. Zhang, C. Huang, and X. Zhou, "Direct Imaging of Pulmonary Gas Exchange With Hyperpolarized Xenon MRI," *Innovation* 5, no. 6 (2024): 100720.

35. N. J. Stewart, G. Leung, G. Norquay, et al., "Experimental Validation of the Hyperpolarized $^{129}$Xe Chemical Shift Saturation Recovery Technique in Healthy Volunteers and Subjects With Interstitial Lung Disease," *Magnetic Resonance in Medicine* 74, no. 1 (2015): 196–207.




15222594, 0, Downloaded from https://onlinelibrary.wiley.com/doi/10.1002/mrm.70279 by Huazhong University Of Science, Wiley Online Library on [01/02/2026]. See the Terms and Conditions (https://onlinelibrary.wiley.com/terms-and-conditions) on Wiley Online Library for rules of use; OA articles are governed by the applicable Creative Commons License

36. H. Li, Z. Zhang, X. Zhao, et al., "Quantitative Evaluation of Pulmonary Gas-Exchange Function Using Hyperpolarized $^{129}$Xe CEST MRS and MRI," *NMR in Biomedicine* 31, no. 9 (2018): e3961.

37. J. H. Pilgrim-Morris, G. J. Collier, R. S. Munro, et al., "Compressed Sensing Reconstruction for High-SNR, Rapid Dissolved $^{129}$Xe Gas Exchange MRI," *Magnetic Resonance in Medicine* 93, no. 2 (2025): 741–750.

38. S. Mansson, J. Wolber, B. Driehuys, P. Wollmer, and K. Golman, "Characterization of Diffusing Capacity and Perfusion of the Rat Lung in a Lipopolysaccaride Disease Model Using Hyperpolarized $^{129}$Xe," *Magnetic Resonance in Medicine* 50, no. 6 (2003): 1170–1179.

39. B. B. Moore and C. M. Hogaboam, "Murine Models of Pulmonary Fibrosis," *American Journal of Physiology. Lung Cellular and Molecular Physiology* 294, no. 2 (2008): L152–L160.

40. M. Zhang, H. Li, H. Li, et al., "Quantitative Evaluation of Lung Injury Caused by $PM_{2.5}$ Using Hyperpolarized Gas Magnetic Resonance," *Magnetic Resonance in Medicine* 84, no. 2 (2020): 569–578.

41. H. Li, Z. Zhang, X. Zhao, X. Sun, C. Ye, and X. Zhou, "Quantitative Evaluation of Radiation-Induced Lung Injury With Hyperpolarized Xenon Magnetic Resonance," *Magnetic Resonance in Medicine* 76, no. 2 (2016): 408–416.

42. J. Pauly, P. Le Roux, D. Nishimura, and A. Macovski, "Parameter Relations for the Shinnar-Le Roux Selective Excitation Pulse Design Algorithm (NMR Imaging)," *IEEE Transactions on Medical Imaging* 10, no. 1 (1991): 53–65.

43. Y. V. Chang, J. D. Quirk, I. C. Ruset, J. J. Atkinson, F. W. Hersman, and J. C. Woods, "Quantification of Human Lung Structure and Physiology Using Hyperpolarized $^{129}$Xe," *Magnetic Resonance in Medicine* 71, no. 1 (2014): 339–344.

44. Z. J. Pua, B. S. Stonestreet, A. Cullen, A. Shahsafaei, G. B. Sadowska, and M. E. Sunday, "Histochemical Analyses of Altered Fetal Lung Development Following Single vs Multiple Courses of Antenatal Steroids," *Journal of Histochemistry and Cytochemistry* 53, no. 12 (2005): 1469–1479.

45. J. C. Woods, C. K. Choong, D. A. Yablonskiy, et al., "Hyperpolarized $^{3}$He Diffusion MRI and Histology in Pulmonary Emphysema," *Magnetic Resonance in Medicine* 56, no. 6 (2006): 1293–1300.

46. A. V. Gaikwad, W. Lu, S. Dey, et al., "Vascular Remodelling in Idiopathic Pulmonary Fibrosis Patients and Its Detrimental Effect on Lung Physiology: Potential Role of Endothelial-to-Mesenchymal Transition," *ERJ Open Research* 8, no. 1 (2022): 00571-2021.

47. S. Barratt and A. Millar, "Vascular Remodelling in the Pathogenesis of Idiopathic Pulmonary Fibrosis," *QJM: An International Journal of Medicine* 107, no. 7 (2014): 515–519.

48. D. E. Schraufnagel, D. Mehta, R. Harshbarger, K. Treviranus, and N. Wang, "Capillary Remodeling in Bleomycin-Induced Pulmonary Fibrosis," *American Journal of Pathology* 125, no. 1 (1986): 97.

49. K. Y. Kwon, K. K. Park, and E. S. Chang, "Scanning Electron Microscopic Study of Capillary Change in Bleomycin-Induced Pulmonary Fibrosis," *Journal of Korean Medical Science* 6, no. 3 (1991): 234–245.

50. L. Knudsen, C. Ruppert, and M. Ochs, "Tissue Remodelling in Pulmonary Fibrosis," *Cell and Tissue Research* 367 (2017): 607–626.

51. A. D. Hahn, K. J. Carey, G. P. Barton, et al., "Functional Xenon-129 Magnetic Resonance Imaging Response to Antifibrotic Treatment in Idiopathic Pulmonary Fibrosis," *ERJ Open Research* 9, no. 3 (2023): 00080–02023.

52. A. D. Hahn, K. J. Carey, G. P. Barton, et al., "Hyperpolarized $^{129}$Xe MR Spectroscopy in the Lung Shows 1-Year Reduced Function in Idiopathic Pulmonary Fibrosis," *Radiology* 305, no. 3 (2022): 688–696.

53. A. Bechtel, J. Lu, D. Mummy, et al., "Establishing a Hemoglobin Adjustment for $^{129}$Xe Gas Exchange MRI and MRS," *Magnetic Resonance in Medicine* 90, no. 4 (2023): 1555–1568.

54. R. K. Braun, O. Broytman, F. M. Braun, et al., "Chronic Intermittent Hypoxia Worsens Bleomycin-Induced Lung Fibrosis in Rats," *Respiratory Physiology & Neurobiology* 256 (2018): 97–108.

55. X. Yu, Y. Zhang, X. Yang, et al., "The Influence of BuqiHuoxueTongluo Formula on Histopathology and Pulmonary Function Test in Bleomycin-Induced Idiopathic Pulmonary Fibrosis in Rats," *Evidence-Based Complementary and Alternative Medicine* 2018, no. 1 (2018): 8903021.

## Supporting Information

Additional supporting information can be found online in the Supporting Information section. **Figure S1:** Temporal profiles of the SLR1 and SLR2 pulses and their frequency-domain excitation profiles. The yellow line represents the $^{129}$Xe MR signal, while the blue and red lines represent the $M_z$ and $M_{xy}$ profiles of the pulse excitation in the frequency domain, respectively. The purple line shows the measured frequency response of the pulse on a water phantom. **Figure S2:** The $S_{\mathrm{Mem}}/S_{\mathrm{Gas}}$ ratio as a function of exchange time for both eCSSR and rCSSR sequences. In eCSSR, the ratio increases progressively with exchange time, whereas in rCSSR, it shows an initial dip at very short exchange times before gradually rising.



15222594, 0, Downloaded from https://onlinelibrary.wiley.com/doi/10.1002/mrm.70279 by Huazhong University Of Science, Wiley Online Library on [01/02/2026]. See the Terms and Conditions (https://onlinelibrary.wiley.com/terms-and-conditions) on Wiley Online Library for rules of use; OA articles are governed by the applicable Creative Commons License